References

Case, RB. & Greenberg, H. 1976. The response of canine coronary vascular resistance to local alterations in coronary arterial P CO2. *Circ Res* **39**, 558-66.

Feinberg, H., Gerola, A. & Katz, LN. 1960. Effect of changes in blood CO2 level on coronary flow and myocardial O2 consumption. *Am J Physiol* **199**, 349-354.

Iida, H., Kanno, I., Takahashi, A., Miura, S., Murakami, M., Takahashi, K., Ono, Y., Shishido, F., Inugami, A., Tamura, N., & Tomura, N. 1988. Measurement of absolute myocardial blood flow with H215O and dynamic positron-emission tomography. Strategy for quantification in relation to the partial-volume effect. *Circulation* **78**,104-115.

Iida, H., Miura, S., Shoji, Y., Ogawa, T., Kado, H., Narita, Y., Hatazawa, J., Eberl, S., Kanno, I. & Uemura, K. 1998. Non-invasive quantitation of CBF using oxygen-15-water and a dual-PET system. *J Nucl Med* **39**, 1789-1798.

Iida, H., Rhodes, CG., de Silva, R., Araujo, LI., Bloomfield, PM., Lammertsma, AA., & Jones, T. 1992. Use of the left ventricular time-activity curve as a noninvasive input function in dynamic oxygen-15-water positron emission tomography. J Nucl Med **33**,1669-1677.

Ito, H., Kinoshita, T., Tamura, Y., Yokoyama, I. & Iida, H. 2000. Effect of intravenous dipyridamole on cerebral blood flow in humans. A PET Study. *Stroke* **30**, 1616-1620.

Ito, H., Yokoyama, I., Iida, H., Kinoshita, T., Hatazawa, J., Shimosegawa, E., Okudera, T. & Kanno, I. 2000. Regional differences in cerebral vascular response to PaCO2 changes in humans measured by PET. *J Cerebral Blood Flow and Metab* **20**, 1264-1270.

Ito, H., Yokoyama, I., Tamura, Y., Kinoshita, T., Hatazawa, J., Kawashima, R. & Iida, H. 2002. Regional changes in human cerebral blood flow during dipyridamole stress: Neural activation in the thalamus and prefrontal cortex. Neuroimage **16**, 788-793.

Kazmaier, S., Weyland, A., Buhre, W., Stephan, H., Rieke, H., Filoda, K. & Sonntag, H. Effects of respiratory alkalosis and acidosis on myocardial blood flow and metabolism in patients with coronary artery disease. *Anesthesiology* **89**, 831-837.

Kety, SS. & Schmidt, CF. 1948. The effects of altered arterial tensions of carbon dioxide and oxygen on cerebral blood flow and cerebral oxygen consumption of normal young men. *J Clin Invest* **27**, 484-492.

Kuwabara, Y., Ichiya, Y., Sasaki, M., Yoshida, T., Masuda, K., Matsushima, T. & Fukui, M. 1997. Response to hypercapnia in moyamoya disease. Cerebrovascular response to hypercapnia in pediatric and adult patients with moyamoya disease. *Stroke* **28**, 701-707.

Love, WD., Tyler, MD., Abraham, RE. & Munford, RS. 1965. Effects of O2, CO2, and drugs on estimating coronary blood flow from Rb86 clearance. *Am J Physiol* **208**, 1206-1210.

Neill, WA. & Hattenhauer, M. 1975. Impairment of myocardial O2 supply due to hyperventilation. *Circulation* **52**, 854-858.

Powers, ER., Bannerman, KS., Fitz-James, I., & Cannon, PJ. 1986. Effect of elevations of coronary artery partial pressure of carbon dioxide (PCO2) on coronary blood flow. *J Am Coll Cardiol* **8**, 1175-1181.

Raichle, ME., Martin, WRW., Herscovitch, P., Mintun, MA., & Markham, J. 1983. Brain blood flow measured with intravenous H2(15)O. II. Implementation and validation. *J Nucl Med* **24**, 790-798.

Rowe, GG., Castillo, CA. & Crumpton, CW. 1962. Effects of hyperventilation on systemic and coronary hemodynamics. *Am Heart J* **63**, 67-77.

Shimosegawa, E., Kanno, I., Hatazawa, J., Fujita, H., Iida, H., Miura, S., Murakami, M., Inugami, A., Ogawa, T., Itoh, H., Okudera, T. & Umemura, K. 1995. Photic stimulation study of changing the arterial partial pressure level of carbon dioxide. *J Cereb Blood Flow Metab* **15**, 111-114.

van den Bos, GC., Drake, AJ. & Noble, MI. 1979. The effect of carbon dioxide upon myocardial contractile performance, blood flow and oxygen consumption. *J Physiol* **287**, 149–162.

Wilson, JR., Goldberg, S., Hirshfeld, JW. & Harken, AH. 1981. Effects of respiratory alkalosis on coronary vascular dynamics and myocardial energetics in patients with coronary artery disease. *Am Heart J* **102**, 202-205.

Table 1. Hemodynamics, arterial carbon dioxide tension and pH during $H_2^{15}O$ PET studies

	Rest	Hypercapnea	Hypocapnea
Systolic blood pressure (mmHg)	146.5 ±20.9	159.8 ±25.4	144.8 ±26.7
Diastolic blood pressure (mmHg)	82.8 ±12.0	85.3 ±10.7	78.5 ±13.2
Heart rate (beat / minute)	58.4 ±7.8	61.6 ±8.7	60.7 ±7.8
Rate pressure product	8472 ±1146	9758 ±1609	8717 ±1677
Arterial carbon dioxide tension	40.2 ±2.4	43.1 ±2.7* $	29.2 ±3.4† $
pH	7.417 ±0.013	7.385 ±0.019 $	7.505 ±0.039 $

Data are presented as mean ± standard deviation.

Significance of changes compared with the three groups: *$P<0.05$, †$P<0.01$ by Fisher PLSD,

Significance of changes compared with the resting condition: $P<0.05$, $ $P < 0.01$ by Wilcoxon signed rank test

Table 2. Cerebral blood flow ($mL \cdot minute^{-1} \cdot [100$ gram of perfusable tissue]$^{-1}$), myocardial blood flow ($mL \cdot minute^{-1} \cdot [100$ gram of perfusable tissue]$^{-1}$), and normalized myocardial blood flow ($100 mL \cdot mmHg^{-1} \cdot [heart\text{-}beat]^{-1} \cdot [gram$ of perfusable tissue]$^{-1}$)

	Rest	Hypocapnea	Hypercapnea
Cerebral blood flow	39.8 ±5.3	27.0 ±6.3†	48.4 ±10.4*
Myocardial blood flow	78.2 ±12.6	55.1 ±14.6†	88.7 ±22.4
Normalized myocardial blood flow	93.4 ±16.6	64.5 ±18.3†	90.5 ±14.3

Significance of changes compared with the three groups: $*P < 0.05$, $†P < 0.01$

NOTE

Acceleration of Monte Carlo-based scatter compensation for cardiac SPECT

A Sohlberg[1,2], H Watabe[1] and H Iida[1]

[1] National Cardiovascular Center Research Institute, 5-7-1 Fujishiro-dai, Suita City, 565-8565 Osaka, Japan
[2] HERMES Medical Solutions, Skeppsbron 44, 111 30 Stockholm, Sweden

E-mail: antti.sohlberg@hermesmedical.com

Abstract

Single proton emission computed tomography (SPECT) images are degraded by photon scatter making scatter compensation essential for accurate reconstruction. Reconstruction-based scatter compensation with Monte Carlo (MC) modelling of scatter shows promise for accurate scatter correction, but it is normally hampered by long computation times. The aim of this work was to accelerate the MC-based scatter compensation using coarse grid and intermittent scatter modelling. The acceleration methods were compared to un-accelerated implementation using MC-simulated projection data of the mathematical cardiac torso (MCAT) phantom modelling ^{99m}Tc uptake and clinical myocardial perfusion studies. The results showed that when combined the acceleration methods reduced the reconstruction time for 10 ordered subset expectation maximization (OS-EM) iterations from 56 to 11 min without a significant reduction in image quality indicating that the coarse grid and intermittent scatter modelling are suitable for MC-based scatter compensation in cardiac SPECT.

1. Introduction

The quality of single proton emission computed tomography (SPECT) is degraded by attenuation, collimator blurring and scatter. Whereas attenuation and collimator blurring can nowadays be corrected in clinically acceptable times, accurate and efficient scatter correction has been proven to be a more difficult problem. This is mainly due to the fact that the shape of the scatter point-spread function depends on the location inside the object and can be very difficult to parametrize.

One very promising recently presented scatter compensation method is the Monte Carlo (MC)-based scatter correction by Beekman *et al* (2002). In this method, a MC simulator is used as a forward-projector for scatter in the ordered subset expectation maximization

N277

(OS-EM) algorithm (Hudson and Larkin 1994). MC-based scatter modelling is expected to be especially advantageous in areas where the attenuating media is highly non-uniform such as the thorax, because it can faithfully produce the complex shape of the scatter response function. The MC-based scatter compensation has been shown to outperform the common triple-energy window scatter compensation method in terms of contrast and myocardial lesion detectability (Xiao *et al* 2006). Unfortunately, despite the considerable advances made in MC-based scatter compensation its widespread utilization in clinical practice can still be limited by long computation times.

Kadrmas *et al* (1998) have presented two simple and effective acceleration methods for reconstruction-based scatter compensation. The first of these approaches is the coarse grid scatter modelling method, which calculates the scatter contribution using sparser grid than is used in the actual reconstruction. The second approach is the intermittent scatter modelling method, where scatter is modelled only during the first couple of OS-EM iterations and then held as a constant additive factor for the later iterations. Both of these approaches are based on the assumption that the scatter response contains mainly low-frequency components and can thus be modelled with a relatively large voxel size and not during the last OS-EM iterations. Kadrmas *et al* presented their acceleration methods for the effective scatter source estimation method (Frey and Tsui 1996) and showed that the performance of the accelerated scatter compensation was very similar to the performance of the standard (un-accelerated) scatter correction.

The goal of this work was to implement the coarse grid and intermittent scatter modelling methods for MC-based scatter compensation and to evaluate their performance in case of ^{99m}Tc cardiac SPECT.

2. Materials and methods

2.1. Implementation of the MC simulator

MC simulations are based on sampling radioactive decays within a source volume and following their interactions inside the attenuating media. Our MC simulator uses four different maps in the simulations: emission map for setting photons to be tracked, density map for sampling interactions and primary and scatter maps for storing photon weights. The history of each photon (primary or scatter) in our simple MC simulator is tracked shortly as follows:

(1) If the simulated photon is a primary the primary map is updated. Otherwise direction cosines are sampled and random walk is started for the scatter photon.

(2) Photon interaction points are calculated using the delta scattering algorithm (Woodcock *et al* 1965), which does not require ray tracing through the attenuating media. The basic principle of delta scattering is that the path-length P between two 'fictious' interaction points is sampled as $P = -\ln(R)/\mu_{max}$, where R is a uniform random number and μ_{max} is the largest attenuation coefficient in the attenuating media (Ljungberg *et al* 2005). At the end of the sampled path a possible interaction is sampled according to established methods or tracking is continued by sampling a new distance P according to the above-mentioned equation.

(3) At each real interaction point photon weight is multiplied by the probability that no photoelectric effect occurred and a copy of the original photon is forced to Compton scatter towards the detector and scatter map is updated according to the convolution-based forced detection approach (de Jong *et al* 2001).

(4) If predetermined number of scattering events has not been reached, the history of the original photon is continued by Compton scatter. New direction cosines are sampled from the Klein–Nishina function and tracking is continued from (2).

After all the photons have been simulated the primary and scatter maps are multiplied by probability that photon emitted from a certain voxel reaches the detector without interaction. Then these maps are convolved with depth-dependent detector response function, which is assumed to be Gaussian. The blurred primary and scatter maps are finally forward-projected to primary and scatter projections.

2.2. Implementation of the reconstruction algorithm with MC-based scatter compensation

The developed MC simulator was included into an OS-EM reconstruction algorithm as forward-projector for the scattered counts as originally proposed by Beekman *et al* (2002). The OS-EM is given by

$$f_j^{\text{new}} = \frac{f_j^{\text{old}}}{\sum_{i \in S_n} a_{ij}} \sum_{i \in S_n} a_{ij} \frac{p_i}{\sum_k a_{ik} f_k^{\text{old}} + s_i}, \tag{1}$$

where f is the reconstructed image, p is the measured projections, j (or k) is the reconstruction voxel index, i is the projection pixel index, a_{ij} is the probability that emission from voxel j is detected in pixel i, s is the MC-based scatter projections and S_n is the nth subset. The image update in OS-EM consists of sequential forward- and back-projection operations. The estimated projections are obtained by forward-projecting the current image estimate $\left(\sum_k a_{ik} f_k^{\text{old}}\right)$, and correction terms that are used to update the old image are formed by back-projecting the ratio of the measured and estimated + scatter projections $\left(\sum_{i \in S_n} a_{ij} \frac{p_i}{\sum_k a_{ik} f_k^{\text{old}} + s_i}\right)$.

In this work the forward- and back-projectors were implemented as rotation based (Di Bella *et al* 1996). The back-projector included attenuation and detector response compensation and the forward-projector attenuation, detector response and MC-based scatter compensation. Attenuation correction factors for each voxel were calculated simply by summing the rotated attenuation map along columns. Detector response, on the other hand, was modelled by convolving each plane of the reconstruction matrix parallel to the projection plane with collimator response kernel, which was assumed to be Gaussian. The scatter projection for each projection angle was obtained by MC-based forward-projection of the current image estimate.

2.3. Acceleration of MC-based scatter compensation

The coarse grid scatter modelling method was implemented by simply down-sampling the current image estimate (and the attenuation map) into a sparser matrix before the MC-based forward-projection and linearly interpolating the scatter projections back to the original size after forward-projection was finished. In the intermittent acceleration approach the MC-based scatter modelling is performed only in the few early OS-EM iterations and after that the scatter projections are kept fixed for remaining iterations.

2.4. Performance tests

Performance tests were performed using a female version of the mathematical cardiac torso (MCAT) phantom (Tsui *et al* 1994), and the camera parameters are shown in table 1. The MCAT phantom modelled normal human tissue densities in the thorax region and the source distribution presented the ^{99m}Tc uptake with the following relative activities per
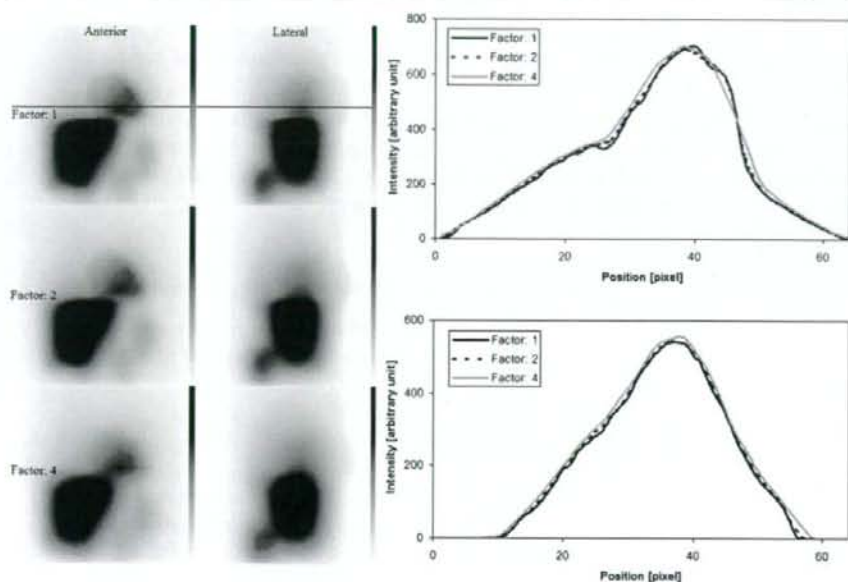
Figure 1. Comparison of scatter projections and profiles obtained with different down-sampling factors (factor: 1 is scatter projection without down-sampling). Upper profile is obtained from the anterior projection and lower from the lateral projection. Locations of the profiles are shown as horizontal lines.

Table 1. Camera parameters for Monte Carlo simulations.

Low-energy high-resolution collimator (4.0 cm hole length, 0.178 cm hole diameter)
0.4 cm intrinsic detector resolution
9.0% energy resolution
15.0% energy window centred on 140 keV
23.0 cm radius of rotation

voxel: myocardium 100, liver 50, kidney 100, spleen 80, lung 5 and rest of the body 2.5. Two lesions (anterior and inferior) with the relative uptake of 2.5 were included in the left myocardium.

The effects of different down-sampling factors in the coarse grid scatter modelling scheme were studied by performing MC simulations using the MCAT phantom. The pixel size was set to 0.625 cm (64×64 projection and $64 \times 64 \times 64$ image matrix size). Down-sampling factors of 2 ($64 \times 64 \times 64$ image matrix down-sampled to $32 \times 32 \times 32$ matrix) and 4 ($64 \times 64 \times 64$ image matrix down-sampled to $16 \times 16 \times 16$ matrix size) were investigated. Figure 1 presents anterior and lateral scatter projection images of the MCAT phantom. According to this figure factor 4 produces slightly distorted scatter projections, and thus the down-sampling factor was set to 2 for all the reconstructions accelerated with the coarse grid scatter modelling.

The effect of the number of scatter update iterations was studied by using MCAT projection data simulated using the SIMIND MC simulator (Ljungberg and Strand 1989). The camera parameters for this simulation are again shown in table 1. The number of simulated noise-free
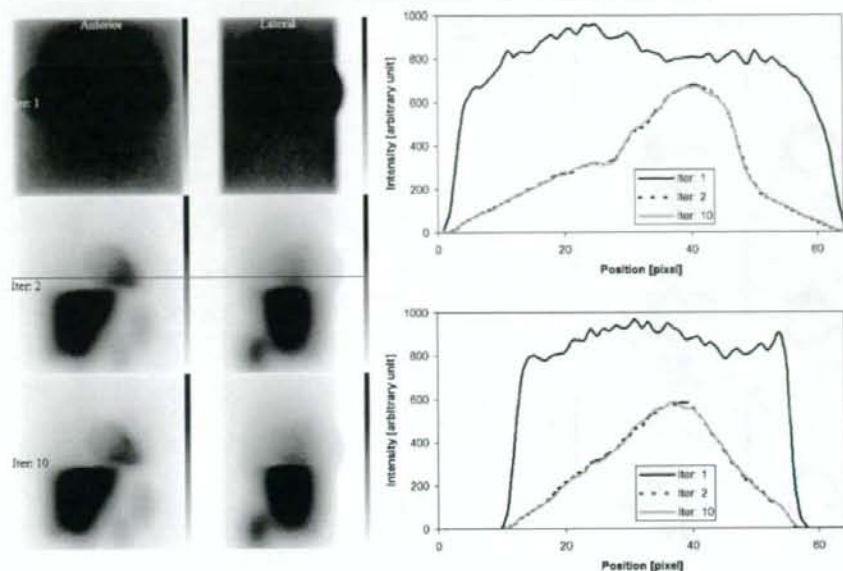
Figure 2. Comparison of different number of scatter update iterations. Upper profile is obtained from the anterior projection and lower from the lateral projection. Locations of the profiles are shown as horizontal lines.

projections was 64 on a 360° orbit and pixel size was 0.3125 cm (128 × 128 projection and 128 × 128 × 128 image matrix size). The projections were collapsed to a 64 × 64 matrix size before the reconstruction. Reconstruction using the noise-free projection data was performed with 16 subsets and 1–10 iterations, and the MC forward-projected scatter projections were saved after every iteration. Figure 2 presents scatter projection images and profiles for different iteration numbers, and these images show that the scatter projections do not change markedly after two iterations. Therefore, in the following performance tests only two scatter iterations were used when intermittent scatter modelling was applied.

The acceleration methods were tested using the same MCAT projection data that were used to find the scatter iterations stopping point. Poisson noise was added to the noise-free projections by setting number of total counts to 5 million. The projections were reconstructed without scatter compensation, with the MC-based scatter compensation but without acceleration, with coarse grid scatter modelling (down-sampling factor of 2), with intermittent scatter modelling (scatter updated during the first two iterations) and with both accelerations applied at the same time. Number of MC simulated photons per projection angle was set to 1.0 million and 16 subsets with 10 iterations were used. After reconstruction images were filtered with a 3D Butterworth filter (order: 5, cutoff: 1.0 cm^{-1}), transverse slices were zoomed and reoriented into short-axis slices. Regions of interest (ROI) were drawn on the normal myocardium, ventricle and on the anterior/inferior defect areas. Normal myocardium to ventricle and normal myocardium to lesion contrasts were calculated.

In addition to Monte Carlo simulations the acceleration methods were also tested using a clinical ^{99m}Tc myocardial stress/rest perfusion study acquired with the Siemens Symbia SPECT/CT scanner. Low-energy high-resolution parallel hole collimators were used, and
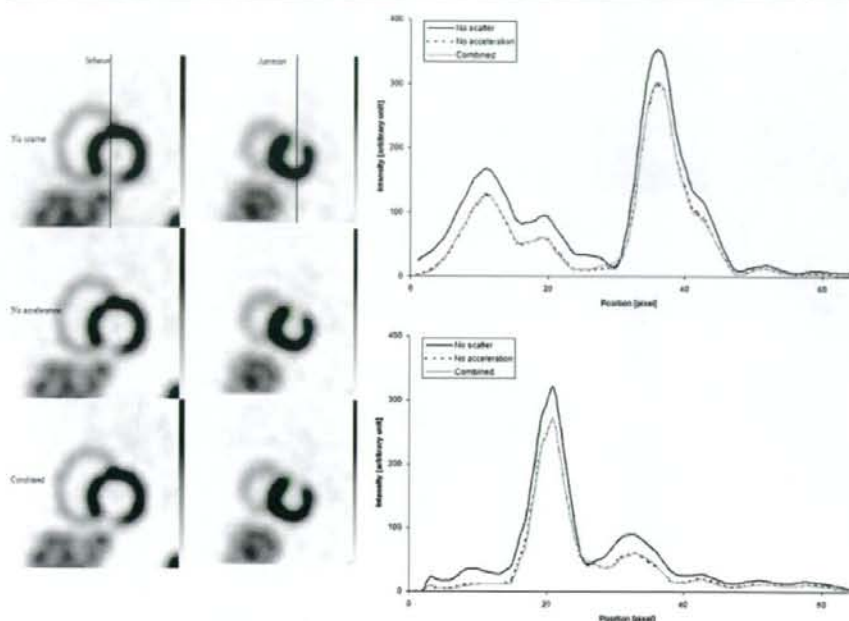
Figure 3. Short-axis slices and profiles through the heart of the MCAT phantom for reconstruction without scatter compensation (no scatter) and with MC-based scatter compensation without acceleration (no acceleration) and with coarse grid + intermittent scatter modelling (combined). Results for other acceleration methods are not shown, because they overlap the coarse grid + intermittent scatter compensation profiles. Upper profile is obtained from the image with inferior lesion and lower with anterior lesion. Locations of the profiles are shown as vertical lines.

Table 2. Lesion-to-normal myocardium and ventricle-to-normal myocardium contrasts for different MC-based scatter compensation acceleration schemes.

Scatter compensation method	Acceleration method	Contrast		
		Anterior	Inferior	Ventricle
No compensation		0.57	0.51	0.80
MC-based	No acceleration	0.64	0.58	0.91
	Coarse grid	0.65	0.59	0.93
	Intermittent	0.62	0.60	0.93
	Coarse grid+intermittent	0.64	0.59	0.93

60 projection angles over a 180° arc were acquired using a symmetric 15% energy window centred at 140 keV.

3. Results

Figure 3 shows short-axis slices and profiles through the left ventricle of the MCAT phantom for reconstruction without scatter compensation and with the MC-based scatter compensation without acceleration and with coarse grid + intermittent scatter modelling. Profiles for the
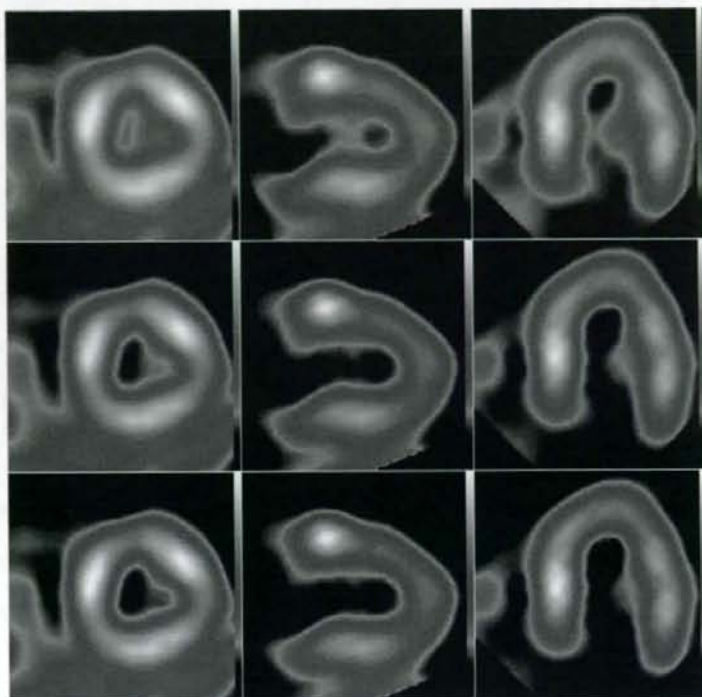
Figure 4. Example short-axis (first column), vertical long-axis (second column) and horizontal long-axis (third column) slices from a clinical rest myocardial perfusion study for reconstruction without scatter compensation (first row), with MC-based scatter compensation without acceleration (second row) and with coarse grid +intermittent scatter modelling (third row).

un-accelerated and accelerated scatter compensation practically overlap indicating similar performance. This same conclusion can also be drawn from table 2, which presents the lesion and ventricle contrasts. All the scatter compensation methods offer very similar contrast values and clearly improve contrast when compared to reconstruction without scatter compensation.

Figure 4 presents results for the resting clinical study (for the stress study the findings in image quality were identical to the resting study). It can be seen that the images reconstructed with and without MC-based scatter compensation acceleration are nearly identical. Table 3 presents the approximate reconstruction times for different scatter compensation methods.

4. Discussion

The aim of this study was to accelerate the MC-based scatter compensation using the coarse grid and intermittent scatter modelling methods. Both of these acceleration methods proved to provide clear improvement in execution times without any marked degradation in image quality when compared to un-accelerated version of MC-based scatter-compensation (tables 2 and 3, figures 3 and 4). The greatest improvement in terms of speed was obtained by combining the two acceleration methods.

Table 3. Approximate reconstruction times (10 iterations, 16 subsets and 1 million photons per projection) for different MC-based scatter compensation acceleration schemes. Reconstructions were performed using 2.33 GHz Pentium processor with 8 GB RAM.

Scatter compensation method	Acceleration method	Time (min)
No compensation		0.8
MC-based	No acceleration	55.6
	Coarse grid	53.4
	Intermittent	11.6
	Coarse grid + intermittent	11.2

The comparison studies for the scatter compensation methods were performed with $64 \times 64 \times 64$ matrix sizes and coarse-grid down-sampling factor of 2 was used, because larger down-sampling factors could not fully preserve the details of the scatter projections (figure 1). With larger matrix sizes than $64 \times 64 \times 64$ larger down-sampling factors could probably be used for higher acceleration. This was not studied in this work, because in the case of cardiac SPECT $64 \times 64 \times 64$ matrix size is usually considered the standard.

The acceleration achieved with the coarse grid scatter modelling depends also on the implementation of the MC simulator that is used in the forward-projection. As mentioned, our MC simulator is based on the delta scattering technique (Woodcock *et al* 1965), which allows calculation of the photon interaction points without time-consuming ray tracing. Therefore, the coarse-grid scatter modelling provided acceleration mainly because the collimator response and attenuation modelling were performed with the sparser matrix. In the case of 1 million simulated photons per projection the time needed to model the collimator response and attenuation is, however, only a small fraction of the time that is spent in sampling the various probability distributions in the MC calculations. Thus the speed-up provided by the coarse-grid scatter modelling is quite small, but can be much greater if a smaller number of simulated photons are used. In addition, if a ray-tracing-based MC algorithm is used instead of delta scattering, coarse-grid scatter modelling will probably increase the speed much more, because the efficiency of ray tracing depends heavily on the matrix size.

In this study the scatter projections were not noticed to change markedly after two iterations, and thus in the intermittent scatter modelling scheme scatter projections were updated only during the first two OS-EM iterations. The number of scatter iterations needed may, however, depend on the imaging situation as mentioned by Kadrmas *et al* (1998) and should therefore be checked before using intermittent scatter modelling as an acceleration method.

One important thing that was not considered in detail in this work is the number of simulated photons per projection. We chose the 1 million photons per projection according to our preliminary studies, where we compared the quality of images reconstructed using different number of simulated photons and noticed that using over 1 million photons per projection does not lead to a significant increase in image quality. The performance of MC-based scatter compensation is, however, quite complicated because it is not only influenced by the number of simulated photons but also by the interplay of noise in attenuation map/projection data and the number of simulated photons. Therefore, a detailed study of noise effects, e.g. similar to the one presented by de Wit *et al* (2005), is probably needed in the future. If different number of photons per projection are to be used the speed-up factors might not be the same as in table 2.

Faster reconstruction times with MC-based scatter compensation than those shown in table 3 have been presented in the literature (e.g. de Wit *et al* (2005) and Xiao *et al* (2006)). This

speed difference is probably mainly related to algorithm implementation. Our reconstruction algorithm is not yet fully optimized, and we believe that we can greatly reduce the execution time of our reconstruction. In addition to direct code optimization, we are also planning to parallelize our code for multi-core processors. The acceleration methods presented in this work should be very suitable for different parallelization schemes, because they do not affect the general structure of the OS-EM reconstruction algorithm.

5. Conclusions

We conclude that both the coarse grid and the intermittent scatter modelling methods are suitable for accelerating MC-based scatter compensation, and with these methods MC-based scatter compensation is a promising alternative for clinical cardiac SPECT.

Acknowledgment

References

Beekman F J, de Jong H W A M and van Geloven S 2002 Efficient fully 3-D iterative SPECT reconstruction with Monte Carlo-based scatter compensation *IEEE Trans. Med. Imaging* 21 867–77

de Jong H W A M, Slijpen E T P and Beekman F J 2001 Acceleration of Monte Carlo SPECT simulation using convolution-based forced detection *IEEE Trans. Nucl. Sci.* 48 58–64

de Wit T C, Xiao J and Beekman F J 2005 Monte Carlo-based statistical SPECT reconstruction: influence of number of photon tracks *IEEE Trans. Nucl. Sci.* 52 1365–9

Di Bella E V R, Barclay A B, Eisner R L and Schafer R W 1996 A comparison of rotation-based methods for iterative reconstruction algorithms *IEEE Trans. Nucl. Sci.* 43 3370–6

Frey E C and Tsui B M W 1996 A new method for modelling the spatially-variant, object dependent scatter response function in SPECT *IEEE Nuclear Science Symp.and Medical Imaging Conf. Record* pp 1082–6

Hudson H M and Larkin R S 1994 Accelerated image reconstruction using ordered subsets of projection data *IEEE Trans. Med. Imaging* 13 601–9

Kadrmas D J, Frey E C, Karimi S S and Tsui B M W 1998 Fast implementations of reconstruction-based scatter compensation in fully 3D SPECT image reconstruction *Phys. Med. Biol.* 43 857–73

Ljungberg M, Larsson A and Johansson L 2005 A New collimator simulation in SIMIND based on the Delta-Scattering technique *IEEE Trans. Nucl. Sci.* 52 1370–5

Ljungberg M and Strand S-E 1989 A Monte Carlo program for the simulation of scintillation camera characteristics *Comput. Methods Programs Biomed.* 29 257–72

Tsui B M W, Zhao X D, Gregoriou G K, Lalush D S, Frey E C, Johnston R E and McCartney W H 1994 Quantitative cardiac SPECT reconstruction with reduced image degradation due to patient anatomy *IEEE Trans. Nucl. Sci.* 41 2838–44

Woodcock E, Murphy T, Hemmings P and Longworth S 1965 Techniques used in the GEM code for Monte Carlo neutronics calculations in reactors and other systems with complex geometry *Proc. Conf. for Applications of Computing Methods to Reactor Problems* p 557

Xiao J, de Wit T C, Staelens S G and Beekman F J 2006 Evaluation of 3D Monte Carlo-based scatter correction for ^{99m}Tc cardiac perfusion SPECT *J. Nucl. Med.* 47 1662–9

ORIGINAL PAPER

Self-organized ZnO nanorod with photooxidative cell membrane perforation enables large-scale cell manipulation

Takashi K. Saito · Munetoshi Seki · Hitoshi Tabata

Abstract Various devices have been developed for verification and application of cellular functions in recent years. In our previous study, we found that local oxidation reactions in the cell membrane could produce submicron sizes of reversible membrane perforations in cells, while more than 80% of treated cells were viable even after perforations; therefore, to date, we have attempted some applications of this mechanism and analyzed their feasibility. In the present study, we developed a rod-shaped device in which the function of membrane perforation is added by utilizing a photosensitizer and, using the device, we have attempted to produce membrane perforations in a large number of cells. Zinc oxide nanorods were synthesized on the basis of the vapor–liquid–solid mechanism and α-terthienyl (photosensitizer) was adsorbed onto gold at the top of the rods to add a membrane perforation function. We studied the effect of the oxidation catalytic ability of the rods on rat PC12 cells after pressing and making the rods' growth side come into contact with the base plate pressed onto the cells in a culture plate followed by photoexcitation

of the photosensitizer for a certain period of time. It was revealed that water-soluble fluorescent marker molecules added extracellularly were taken up by the cells when the rods were applied at a pressure of 70 g/cm^2, with a light intensity of 0.82 W/cm^2, and with light irradiation for 30 s, as found in the case of the conventional photochemical cell membrane perforation method targeted at a single cell. These results suggest that cell membrane perforation can be successfully achieved in a large number of cells at a time.

Introduction

Until recently, a glass microcapillary has been used as a tool for introducing some materials into cells via perforations in the cell membrane and for measuring cell membrane potential. Representative examples of such a capillary include a glass microelectrode [1] and a patch electrode [2]. These electrodes are likely to cause cell death because they mechanically damage cells. This is why the use of conventional microdevices for cell membrane perforation has been limited to basic studies. An important point is that cell membrane perforation cannot be achieved merely by pressing a microdevice with a sharp edge onto a cell because the flexibility and flowability of the cell membrane prevent it from being altered; in some cases, cells may be destroyed if such a device is pressed too hard. On the other hand, the patch electrode, which produces cell membrane perforations through suction instead of the

T. K. Saito (✉)
Department of Bioengineering, School of Engineering,
The University of Tokyo,
2-11-16 Yayoi, Bunkyo-ku,
Tokyo 113-8656, Japan
e-mail: saito@bionano.t.u-tokyo.ac.jp

M. Seki · H. Tabata
Department of Electronic Engineering, School of Engineering,
The University of Tokyo,
7-3-1 Hongo, Bunkyo-ku,
Tokyo 113-8656, Japan

insertion mechanism, is now available in a form of a chip [3]. However, this electrode poses a problem in that its integrated application is difficult since accurate control of suction is necessary when making the electrodes come into contact with individual target cells. As an alternative method for introducing some materials into cells, a cell membrane perforation technique using a focused laser was developed in the 1980s [4]; unfortunately, little has been reported on its progress since then. In our series of studies to develop intracellular electrodes, we found that local use of a photosensitizer resulted in immediate recovery of treated rat PC12 cells [5] within a few minutes even after the cells had been damaged to the extent that the electrical resistance of the cell membrane was reduced to half [6]. On the basis of this finding, we have attempted to apply the phenomenon to an intracellular sensor or a method for intracellular delivery of molecules of interest. The photosensitizer applied, 5,5″-bis(aminomethyl)-2,2′:5′,2″-terthiophene dihydrochloride (BAT) [7], is a water-soluble derivative of α-terthienyl (α-T), which is a photosensitizer of plant origin [8] having an excitation wavelength of 360 nm. Upon collecting corroborative lines of evidence that the mechanism of this transient cell damage is mediated by photooxidation reactions [9], we applied this cell membrane perforation technique to the microinjection method, i.e., an injection method targeted for a cell using a glass microcapillary [10]. In addition, we also found that the injection of functional dye, an antibody, and messenger RNA into primary cultured rat hippocampal pyramidal cells in the nervous system resulted in survival of the treated cells as well as successful manifestation of individual functions of these injected molecules [11]. A notable point of the perforation method is that it is based on autooxidation of cell membrane phospholipids. The chain-reactive autooxidation is a feature of unsaturated fatty acids [12], and the typical related cell membrane components are phosphoglycerides—phosphatidylserine, phosphatidylethanolamine, phosphatidylcholine, and phosphatidylinositol. These molecules are common main components of the cell membrane phospholipids in various cells and contain one unsaturated oleate group, which has one double bond.

The molecular mechanism is described as follows. The double bond is attacked by reactive oxygen species, e.g., catalyzed by a photosensitizer and loss of one hydrogen radical. The dissociated bond forms sequentially a peroxyl radical by addition reaction with free oxygen. The peroxyl radical removes one hydrogen radical from an adjacent double bond and the formation of a carboxyl group leads finally to stabilization. The spatial layout of the membrane phospholipids—each hydrophobic oleate group associates approximately—permits the chain reaction. This chain-reactive oxidation is triggered by a small quantity of the reactive oxygen species, but has a drastic effect on some

properties of the membrane—including the flexibility against physical contacts—after some induction period for the progress of the reaction. Referring to membrane proteins, these molecules could also be oxidized, but could not participate in the chain reaction because the positions of the double bond are not commonly oriented, compared with those of the phospholipids. If the oxidative damage is still limited within the capacity of the antioxidative mechanisms of the processed cell, the cell will recover.

In the present study, we examined whether this cell membrane perforation technique can be carried out on a large scale at low cost as a universal method for cell membrane perforation, and this is the first report. Cell membrane perforation with photochemical reactions can be performed without any precise manipulation procedures to target cells, since it only requires light irradiation while a photosensitizer or a photocatalyst is locally in contact with the target cells. In this point, this technique is intrinsically suitable for large-scale application, in contrast to conventional mechanical or optical perforation methods. For example, a cell membrane perforation device has recently been developed in which the probe of the scanning probe microscope is precisely processed by a focused ion beam [13]. The device is a precise round bar with a maximum diameter of 400 nm and can deliver genes of interest to cells without inducing cell death. A perforation method targeted to a single cell may be favorable in that it does not require any oxidation reactions toxic to cells, compared with the photochemical cell membrane perforation technique. On the other hand, it would be difficult to perform integrated perforation using a focused ion beam in thousands to millions of cells in vivo such as groups of nerve cells because of the high cost and the needle device requires scanning probe microscopes because of their precise nanometer-scale operation.

Another competitive method for intracellular delivery to a large number of cells includes a biological delivery technique using viral vectors or others; however, since its physiological activity upon clinical application is not completely predictable, development of nonbiological techniques is currently expected.

Our proposed membrane-perforation method can be applied for any microstructures, and we have chosen self-organized ZnO nanorods as an adequate example of the process which has enough controllable range of the dimensions for the rods, and has lower cellular toxicity. Some of the features of ZnO nanorods prepared for the present experiments using cells are as follows. They are grown on the basis of the vapor–liquid–solid mechanism [14] and they can bind in a self-assembling fashion to sulfur atoms of thiophene photosensitizers such as BAT and α-T, which was used in the previous studies, since a high concentration of gold remained at the top of the crystals.

Materials and methods

Biochemical/chemical materials

In the present study, α-T (Aldrich) was used as a photosensitizer. We focused on the rat pheochromocytoma cell line, PC12. The cell was obtained from the Riken Bio Resource Center (Ibaraki, Japan) and subcultured as described elsewhere [6] in NeuroBasal medium plus B27 supplement type serum-free culture medium (Invitrogen). The production of perforations in the cell membrane was evaluated on the basis of the cellular uptake of the water-soluble fluorescence dye lucifer yellow CH (LY) (Molecular Probes) [15], which was not supposed to penetrate the cell membrane. Cells (3 ml of suspension at an initial density of 140 cells/μl) were subcultured to a culture plate and, following 3–4 days of incubation, used as target cells for perforation.

ZnO nanorods

In the present study, ZnO nanorods prepared by the pulsed laser deposition technique were used as cell membrane perforation devices. The target ZnO pellet was prepared by the conventional solid-state reaction. A gold thin film with a thickness of 1–3 nm was deposited on the Al_2O_3 (0001) substrate before ZnO deposition. Then the substrate was heated at 973 K and ZnO target was ablated by an ArF excimer laser (wavelength 193 nm) under an oxygen pressure of 1 Pa for nanorod growth. The vapor–liquid–solid mechanism with a gold core would probably account for the growth of the nanorods. Gold which is highly contained at the top of the rods can be modified with a thiophene photosensitizer containing sulfur atoms.

Nanorod modified with a photosensitizer

For the nanorod modification with a photosensitizer, α-T was dissolved at 2 mM concentration in methanol and the ZnO nanorod substrate was immersed for 2 h into the solution in the dark. The self-organizing process enables the tips of the ZnO nanorods to be modified with α-T. After the modification, the substrate was rinsed with water. The scanning electron microscopy image of the ZnO nanorods prepared is shown in Fig. 1. The modification with α-T at the top of the nanorods is also shown schematically in the figure.

Process of cell membrane perforation

The flow chart and schematic view are shown in Fig. 2. The base plate was operated under the inverted fluorescence microscope (IX71, Olympus, Tokyo, Japan). The excitation light from the 100-W mercury lamp of the microscope,
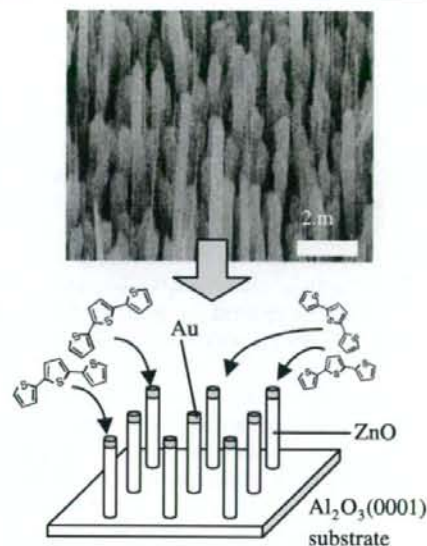

Fig. 1 Scanning electron microscope image of ZnO nanorods and the schematic view of the α-terthienyl-bound nanorod substrate

which was transmitted by a UV excitation filter (type WU), was used for α-T excitation, and a violet filter (type WBV) was used for LY. For the actual experimental procedures, regular culture medium in a culture plate was replaced with medium containing 2 mM LY, and the base plate of the membrane perforation device was positioned to come into contact with and pressed onto the cells. Finally, the photosensitizer was optically excited using the filter for UV-excitation-induced fluorescence. When the cell membrane is successfully perforated, LY added extracellularly can enter the intracellular compartment; then, upon recov-
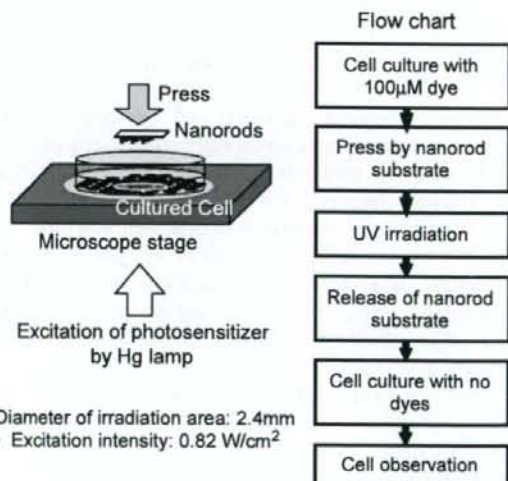

Fig. 2 Large-scale cell membrane perforation process using self-organized nanorods

ery of the membrane from its perforated state, LY can be trapped intracellularly. Following completion of the perforation treatment, the medium containing LY was replaced with fresh culture medium and the number of the cells containing LY in the intracellular compartment was evaluated on the basis of fluorescence signals. The area of the base plate applied was approximately 0.5 cm^2 and pressurization was carried out with a brass square pole with a mass of 35 or 70 g being placed on the plate. Thus, with this modified base plate, a group of PC12 cells attached to a culture plate were pressurized in the pressure range $0–140$ g/cm^2 and light irradiation was used to optically excite the photosensitizer. All experiments were performed at room temperature (298 K).

Quantitative evaluation of perforation efficiency

So far, quantitative evaluation of a large number of cells has been limited to the use of a cell sorter for floating cells; on the other hand, there have been few reports of attempts to quantitatively evaluate the alteration efficiency in cells attached to a culture plate. To quantitatively evaluate the perforation efficiency in a large number of attached cells, we analyzed microscopic transmission and fluorescence images using the image analysis tool ImageJ (NIH, USA).

We superimposed a fluorescence image on the corresponding transmission image, and counted visually the cell numbers to calculate the stained cell ratio. An example of the calculation is shown in Fig. 3. The ratio was calculated in each quadrant that was compartmentalized by the cross
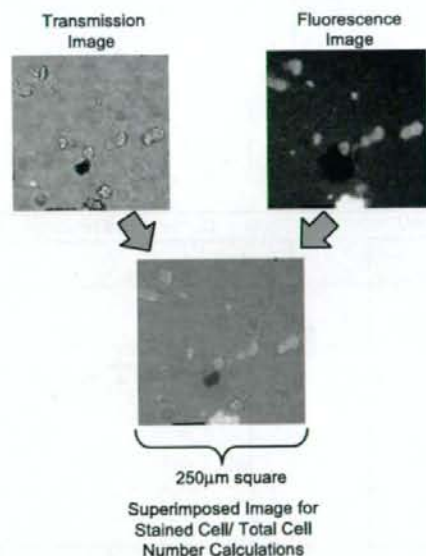
line in the dotted frame shown in Fig. 4, and the average of the four quadrants was presented in the graph.

Results and discussion

Figure 4 shows a photomicrograph of a group of PC12 cells attached to a culture plate following application of the nanorods. In general, similar to the case of the conventional photochemical cell membrane perforation targeted to a single cell, LY added extracellularly was taken up by the cells in the presence of the photosensitizer and excitation light. This suggests that cell membrane perforation was successfully achieved in a large number of cells. A characteristic phenomenon was that whereas fluorescent dye was rarely observed in the intracellular compartment when nanorods of 500–600-nm diameter were applied at a pressure of 70 /cm^2 without light irradiation, the uptake efficiency of the fluorescent dye reached almost 100% when there was light irradiation for 30 s. Although similar perforations could be produced at a pressure of 140 g/cm^2, the number of visible cells decreased. In contrast, when nanorods of 200-nm diameter were applied at a pressure of $70–140$ g/cm^2, cellular uptake of fluorescent dye was not dependent on the time of light irradiation while perforations

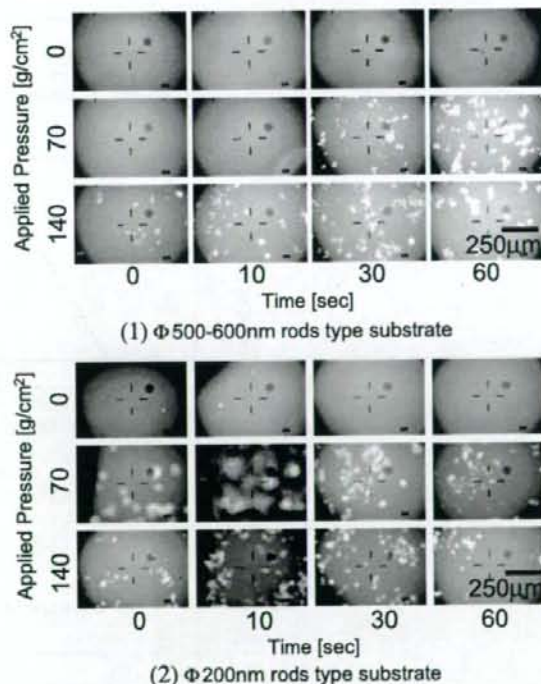Fig. 3 Examples of quantitative estimation of cell perforation by ZnO nanorod substrates

Fig. 4 Pressure and excitation time dependence of cell membrane perforation

were being produced. With both type of nanorods, the 140 g/cm^2 pressure applied cells became flat, and the cells processed with the nanorods of 500–600-nm diameter and 10–60-s irradiation could not be counted because of the excessive change of the shape.

Figure 5 shows the results of image analyses for examining the tendency found in the abovementioned experiments. The range of the projected area shown by the bars in the graph represents the range between minimum and maximum ratios of the projected areas in the four (first to fourth) quadrants of the measurement regions at the described time of light irradiation. Nevertheless, significant differences were obtained on the basis of the

average of all the quadrants, enabling a better understanding of the overall tendency.

There are two characteristics in the cell membrane perforation with photochemical reactions: dependency on light intensity and dependency on the distance between photosensitizers and cells. From this point of view, the nanorods of 500–600-nm diameter had a photochemical characteristic in their perforation style, whereas the nanorods of 200-nm diameter showed a mechanical characteristic in their perforation style since efficiency was not dependent on light intensity. This finding is consistent with the recent report of Han [16] and that of Knoblauch [17] that mechanical cell membrane perforations were produced

Fig. 5 The efficiency of cell membrane perforation for nanorods with different diameters. *LY* lucifer yellow CH
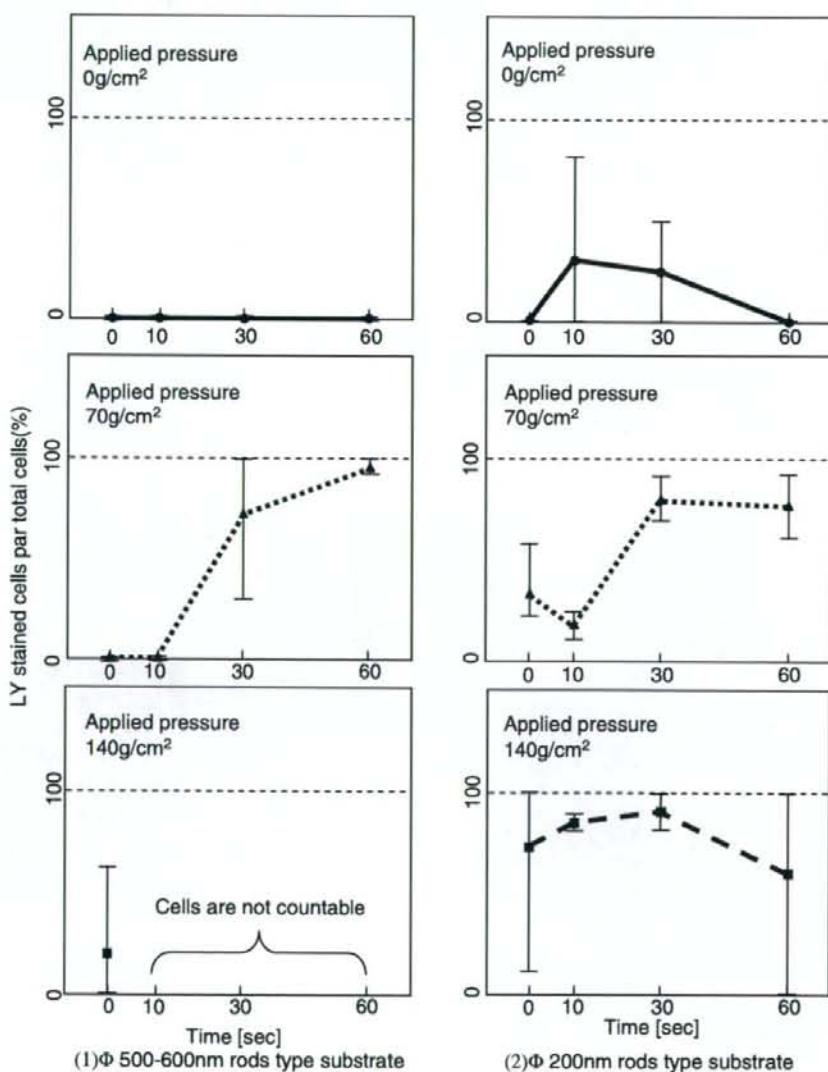
by a microdevice of a few hundred nanometers in diameter. However, in the case of such mechanical cell membrane perforation, it has been demonstrated that high-precision fabricating and operating devices are necessary to maintain subsequent cellular viability even if transient perforations can be successfully produced; for example, the membrane perforation device must meet both conditions that the taper angle of circular cylinder parts of the device should be 0° and that the shape of its top part should be flat. Considering this point, further careful examinations of cellular viability are necessary following membrane perforation using nanorods, in which variations in shape cannot be avoided. Moreover, even if their application to cells is performed by a nanometer-scale controlled manipulator, e.g., which is based on scanning probe microscopes, each perforation process of a needle and a cell should be probabilistic because there is no practical million or billion number scaled multineedle controller.

The decrease in the number of cells found at a pressure of 140 g/cm^2 could be a result of the cells being punctured by the excessive pressure, or being detached from the surface of the culture plate owing to the superfluous close contact between the cells and the plate when the base plate was removed, rather than the detachment of the cells being enhanced by the photochemical reactions. Although successful perforation was achieved at a pressure of 70 g/cm^2, problems such as adsorption of target cells to a cell manipulation tool and detachment of cells from a culture plate, which frequently occur in mechanical cellular treatments using cell manipulation tools including a capillary, were not observed at the sites of light irradiation. This is also identical to the features of chemical cell membrane perforation methods utilizing membrane degeneration.

Furthermore, a large variation was observed in the plot of the present quantitative evaluation. We suppose the reason for the variations of the stained cell ratios mainly arises from the variations in the number of the cells lying in the individual quadrants of a culture plate largely affecting the range of the projected area. The diameter of the PC12 cell is 10–15 μm, and each cell would suffer a multiple number of impacts by the tip of the rods (Fig. 1); hence the variation comes from the fact that the rods might be averaged on a cell level and could have little affect on a group of cells. In addition, the visual quantitative evaluation was presumably influenced by the fact that the fluorescence intensity in the stained cells was not homogenous.

To overcome these problems, instead of using such obscure transmission images, the double fluorescence staining method, in which the entire population of cells is stained with another fluorescent dye in addition to the fluorescent dye used for evaluating membrane perforation, would be useful to clearly distinguish whole cells and cells affected by perforation. Furthermore, in the present study,

we did not take into consideration differences in fluorescence intensity in individual cells, and it should be possible to improve the quality of quantitative evaluation by carefully analyzing images, including for factors such as fluorescence intensity, in future studies.

Conclusions

A highly efficient cell membrane perforation technique was carried out on a large scale using self-assembled materials. By making photosensitizer-modified ZnO nanorods come into contact with target cells followed by photoexcitation using a photosensitizer, a fluorescent dye that was not supposed to permeate the cell membrane was taken up by the cells. This cellular uptake process was dependent on the fluorescence intensity used for excitation; this dependency is typical to a cell membrane perforation method using photosensitization. In future studies, we should alter or replace the photosensitizer to reduce the potential mutagenesis by the UV irradiation for the excitation, and could employ a medically endorsed photosensitizer which can be excited in the visible to IR [18]. Referring to our former efforts at single-cell processing, we could obtain a cell viability of approximately 90% 3 days after the injection [10], but we have been faced some technical difficulties regarding the long-term traceability of the mass-processed cells, as a result of the drastic increase of the number of cells. Hence, we will improve the cell-tracking functions of the microscope system to evaluate the long-term viability of the processed cell groups. These trials will enable us to develop practical applications of cell treatment techniques using oxide materials, which are excellent in terms of mass productivity.

References

1. Hodgkin AL, Huxley AF (1952) J Physiol 117(4):500
2. Neher E, Sakmann B (1976) Nature 260:799
3. Titiyal JS, Ray M, Sharma N, Rsinha, Vajpayee RB (2002) Cornea 21(6):615
4. Kurata S, Tsukakoshi M, Kasuya T, Ikawa Y (1986) Exp Cell Res 162:372
5. Greene LA, Tischler AS (1976) Proc Natl Acad Sci USA 73:2424
6. Saito T, Hartell NA, Muguruma H, Hotta S, Sasaki S, Ito M, Karube I (1998) Photochem Photobiol 68:745

7. Muguruma H, Saito T, Sasaki S, Hotta S, Karube I (1996) J Heterocycl Chem 33:1
8. Bakker J, Gommers FJ, Nieuwenhuis I, Wynberg H (1979) J Biol Chem 254:1841
9. Saito TK, Takahashi M, Muguruma H, Niki E, Mabuchi K (2001) J Photochem Photobiol B Biol 61:114
10. Saito TK, Muguruma H, Mabuchi K (2002) Biotechnol Lett 24:309
11. Yano R, Okada D, Yap CC, Mabuchi K, Muguruma H, Saito TK (2002) Neuroreport 13:1263
12. Hailliwell B, Gutteridge JMC (1985) Free radicals in biology and medicine. Oxford University Press, Oxford
13. Obataya I, Nakamura C, Han S, Nakamura N, Miyake J (2005) Nano Lett 5(1):27
14. Huang MH, Mao S, Feick H, Yan H, Wu Y, Kind H, Weber E, Russo R, Yang P (2001) Science 292:1897
15. Pochapin MB, Sanger JM, Sanger JW (1983) Cell Tissue Res 234:309
16. Han S, Nakamura C, Obtaya I, Nakamure N, Miyake J (2005) Biochem Biophys Res Commun 332:633
17. Knoblauch M, Hibberd JM, Gray JC, van Bel AJE (1999) Nat Biotechnol 17:906
18. Fisher AMR, Murphree AL, Gomer CJ (1995) Lasers Surg Med 17:2